JOURNAL OF SPACECRAFT AND ROCKETS
Vol. 46, No. 4, July–August 2009

Thermal Analysis of the Radiometer Onboard a Geostationary Satellite

Zhenyu Liu* and Huier Cheng
Shanghai Jiaotong University, 200240 Shanghai, People's Republic of China
and
Jingliang Sun
Shanghai Academy of Spaceflight Technology, 200235 Shanghai, People's Republic of China

DOI: 10.2514/1.40960

In this paper, a detailed thermal model of the radiometer onboard a geostationary satellite is established and transient analyses are performed to obtain the temperature response of a scan mirror and a telescope secondary mirror assembly. The temperature distributions of the radiometer instruments are calculated based on an advanced finite difference method with control volume approach, which can deal with the radiation boundary condition efficiently. Oppenheim's method is used to calculate the radiation heat transfer inside the radiometer, and the calculation of radiation view factor of boundary surface is based on a blockage criterion. The thermal control design for the radiometer is presented, which contributes to its channel registration and focus stability. The thermal consideration for the scan mirror is discussed to obtain acceptable temperature range, which directly affects the performance of the radiometer. The results show that the scan mirror temperature can be reduced to a low level, obviously after appropriate structure design is adopted and a thermal coating is applied on it. The peak temperature of the scan mirror and secondary mirror assembly occurs during the period of the local middle night when they are exposed to the direct view of the sun. The temperature variations of radiometer key instruments are given for several typical solar declinations.

Nomenclature

A	=	area, m^2
A'	=	illuminated area of surface element, m^2
c	=	heat capacity, $J/(kg \cdot K)$
F, F_s	=	view factors, dimensionless
G	=	conductance between calculation points, W/K
g	=	conductance between boundary elements, W/K
k	=	thermal conductivity, $W/(m^2 \cdot K)$
L	=	length of boundary element, m
Q	=	heat flow, W
Q_b	=	heat flow across the control volume boundary, W
Q_0	=	heat generated within the control volume, W
q	=	heat flow across boundary, W
q_s	=	solar constant, W/m^2
R	=	distance between two surfaces, m
T	=	temperature, K
t	=	time, s
U	=	internal energy, J
V	=	volume, m^3
x, y, z	=	coordinates, m
α, β, γ	=	angle between the normal vector and the axis of coordinates, deg
δ	=	element thickness, m
ε	=	emissivity, , dimensionless
θ	=	angle between the element surface normal and the solar vector, deg
ρ	=	density, kg/m^3
σ	=	Stefan–Boltzmann constant, $W/(m^2 \cdot K^4)$
ϕ	=	angle between the element surface normal and the connecting line, deg

Subscripts

b	=	boundary element
CG	=	element center (center of gravity)
i, j	=	ith and jth element or calculation point

Received 12 September 2008; revision received 21 March 2009; accepted for publication 7 April 2009. Copyright © 2009 by the American Institute of Aeronautics and Astronautics, Inc. All rights reserved. Copies of this paper may be made for personal or internal use, on condition that the copier pay the $10.00 per-copy fee to the Copyright Clearance Center, Inc., 222 Rosewood Drive, Danvers, MA 01923; include the code 0022-4650/09 and $10.00 in correspondence with the CCC.

*School of Mechanical Engineering; eric_liu@sjtu.org.

I. Introduction

THE FengYun-4 (FY-4) is China's second-generation geosynchronous meteorological satellite, currently under development, and the first experimental satellite FY-4A is to be launched in 2012. The three-axis body-stabilized spacecraft design of the FY-4 enables the sensors to "stare" at the Earth and thus more frequently image clouds and monitor Earth's surface temperature and water vapor fields. The multichannel scan imaging radiometer is the primary payload for the FY-4, which is designed to sense the radiant and solar reflected energy from sampled areas of the Earth by means of one mirror scan system in conjunction with a Cassegrain telescope. The radiometer is required to operate 24 h a day in a very harsh thermal environment. During a single diurnal period, the optics are exposed to the direct view of the sun for approximately 4 h during the day and the deep space during the remaining periods [1–4]. Even with the highly reflective optical surfaces, the scan mirrors still experience large temperature excursions during the heating and cooling periods [5]. An enormous amount of solar energy can be focused on the secondary mirror assembly when operating normally in the vicinity of the sun, and the telescope secondary mirror temperature may exceed the qualification limits [6,7].

Some general aspects of the thermal design and analysis of the radiometer are presented by Shen et al. [8] and Mahan et al. [9], and the finite element method (FEM) was employed to calculate the temperature distribution of the radiometer. The FEM deals with the radiation boundary condition inefficiently, which is not suitable for the complicated radiation heat transfer calculation in this case. The engineers developing the FY-4 prototype also established a thermal model based on the lumped parameter method to get the thermal response of the radiometer, but the temperature distribution of the radiometer is not very detailed. In this paper, the thermal model based on an advanced finite difference method with control volume

approach is established to give the transient response of the radiometer and detailed temperature distributions of the radiometer instruments. The calculation of conductances between the element center [center of gravity (c.g.)] and element boundary is deduced, which is used in the process of formulating the discrete finite difference equation. The calculation methods of the radiation view factor and solar load are presented, which use an exact contour integral method and the finite difference method with element subdivision based on a blockage criterion. The thermal control system of the radiometer with a detailed thermal design for the scan mirror is presented, which uses appropriate active and passive thermal controls according to the operating characteristics of the radiometer on the geostationary orbit. The thermal analysis results show that the radiometer temperature can be deduced to an acceptable range after thermal control is applied. Finally, a thermal analysis with different solar declinations is performed to get the temperature variations of the radiometer instruments during a whole year, which contributes to determining the operating constraint for the FY-4 design.

II. Thermal Consideration for Radiometer

A. Thermal Control System

The performance of the radiometer is maintained by restricting its total temperature range [10]. The radiometer is thermally isolated as much as possible from the main spacecraft structure. A radiator is used to control the temperature when direct solar flux is received through the scanner aperture. Electrical heaters on the base plate are working to compensate the infrared energy loss to space through the scanner aperture during the cold portion of the diurnal cycle, and heat pipes are used to reduce the temperature difference on the base plate. Additionally, a sun shield is provided around the scan aperture to block incident solar fluxes into the radiometer, which can limit the time in a synchronous orbit day when the scanner receives direct solar radiation. The electrical heat decreases the temperature excursions during the cold part of the daily cycle, but increases the average temperature during the whole daily cycle. To obtain lower temperature ranges, louver-controlled cooling is provided during the direct sunlight portion of the orbit that has a sun shield installed on the Earth end to reduce incident radiation. Multilayer insulation material is applied on the outside of all but the north side of the radiometer to reduce the energy loss to the space. The thermal control of the scan mirror, the telescope assembly along with the base plate, and all structural sidewalls are treated separately from the radiant cooler assembly, which are considered to be thermally isolated from each other.

B. Scan Mirror Thermal Design

The goal of the thermal design is to make the scanning mirror insensitive to the environment as much as possible, so that the mirror will not cause distortions due to the varying temperature conditions [11,12]. The combination of the material and structure is the feature that defines the mirror's structural and thermal characteristics. The mirror material must be precisely selected for the application, because factors such as modulus of elasticity, coefficient of thermal expansion, density, specific heat, and thermal conductivity vary greatly for available materials [13,14]. Table 1 shows a comparison for some material available for fabricating mirrors. In this case, the beryllium scan mirror will be used for the scanning system with minimum inertia requirements. The advantages are lightweight, stiff, thermally stable, highly conductive, and producible design.

Table 1 Typical properties of mirror materials

Material property	Be	SiC	ULE	Al
Elastic modulus, GPa	280	460	66	70
Coefficient of thermal expansion, ppm/K	11.5	2.6	0.08	23.5
Denisty, g/cm^3	1.85	2.8	2.2	2.7
Thermal conductivity, W/(m^2 · K)	194	156	1.3	180
Specific heat, J/(kg · K)	1820	672	770	960

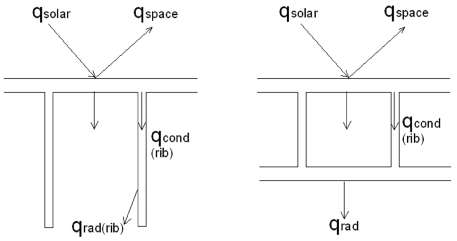

a) Open-back mirror b) Closed-back mirror

Fig. 1 Scan mirror thermal design.

The thermal designs with energy flow for the open- and closed-back mirrors can be seen in Fig. 1. The energy flow for the closed-back mirror has to pass through the rib and then can be radiated through the mirror back surface, which has a higher thermal resistance and will make the scan mirror hot. The open-back mirror design has a temperature stability advantage over the closed-back mirror design because its heat flow is radiated from the mirror back surface directly. The open-back triangular cell scan mirrors would be used for a precision spaceborne radiometer for the FY-4 positioned in a geostationary Earth orbit, as shown in Fig. 2.

The thermal control coatings are used to minimize the temperature excursion. The open-back mirror design has an optical coating on the front surface, and the bottom of the cells is coated with a high-emissivity material such as black paint. The ribs have a low-emissivity coating, and the energy absorbed by the front surface will be rejected with a minimum through-thickness gradient. The scan mirror was found to be very sensitive to radial type gradients. A high-emissivity perimeter coating was changed to a low-emissivity coating, to prevent any type of energy flow from the perimeter of the mirror.

III. Thermal Analysis

The calculation model used for the radiometer thermal analysis is shown in Fig. 3. The thermal model includes all of the radiometer components: scan mirror, secondary mirror assembly (Fig. 4), radiant cooler, and louver. This model requires radiation heat transfer, solar loads, and linear conductors to be calculated. Tables 2 and 3 present the optical properties and the material properties used in the thermal analysis.

In this paper, a control volume approach is used in formulating the discrete finite difference equation, which approximates the temperature governing partial differential equations based on the conservation of energy. This technique involves meshing of the model into control volume regions. Within each region, a calculation point is established at each element's center of gravity. Heat balance

Fig. 2 Scan mirror design for FY-4(520 × 330 mm).

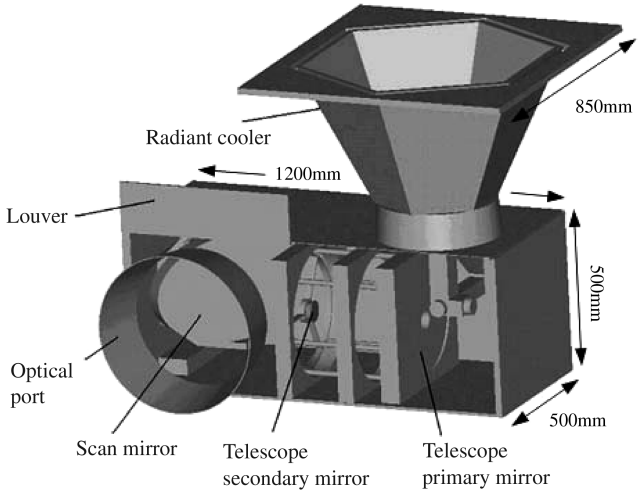

Fig. 3 3-D model of radiometer structure.

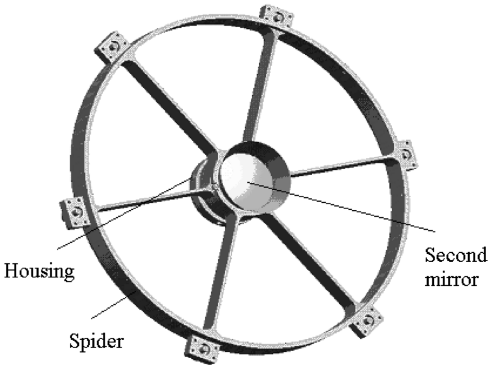

Fig. 4 Secondary mirror assembly.

equations are established for each of these control volumes. The general heat balance equation for a control volume is as follows:

$$Q_b + Q_0 = \frac{dU}{dt} \tag{1}$$

where Q_b is the heat flow across the control volume boundaries, Q_0 is the heat generated within the control volume, and U is the energy stored within the region. Equation (1) not only applies to the control volume, but also to the entire problem domain. The heat flow between two calculation points is characterized by a conductance $G_{i,j}$, as in Fig. 5:

$$Q_{ij} = G_{i,j} \times f(T_i, T_j) \tag{2}$$

Table 2 Optical properties used in the model

Property	Emittance	Solar absorptance
Black paint	0.87	0.95
White paint	0.93	0.13
Scan mirror	0.05	0.05
Primary mirror	0.05	0.05
Secondary mirror	0.05	0.05

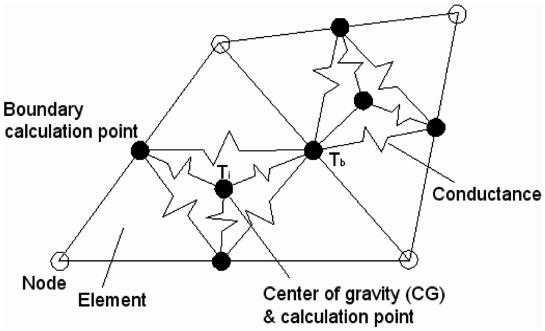

Fig. 5 Conductance between two elements' calculation points.

The temperatures T_i and T_j are evaluated at the control volume calculation points. For a linear conductive conductance, G is a constant value and the heat flow is proportional to the finite difference calculation-point temperature difference. Radiative and other nonlinear conductances involve more complicated functions of temperature.

For a triangular element, a linear internal temperature field is assumed within the element:

$$T(x, y) = m_1 + m_2 x + m_3 y \tag{3}$$

The boundary calculation temperature T_{b_i} is defined at the midpoint of the edge:

$$T(x_{b_i}, y_{b_i}) = T_{b_i} \qquad (i = 1, 2, 3) \tag{4}$$

Substituting the boundary calculation temperatures into the temperature field equation, the coefficients m_1, m_2, and m_3 can be evaluated:

$$\begin{bmatrix} m_1 \\ m_2 \\ m_3 \end{bmatrix} = \begin{bmatrix} n_{11} & n_{12} & n_{13} \\ n_{21} & n_{22} & n_{23} \\ n_{31} & n_{32} & n_{33} \end{bmatrix} \begin{bmatrix} T_{b1} \\ T_{b2} \\ T_{b3} \end{bmatrix} \tag{5}$$

The unit edge normal vectors $\boldsymbol{N}_i$ at the boundary elements can be evaluated:

$$\boldsymbol{N}_i(x_{b_i}, y_{b_i}) = c_i \boldsymbol{i} + d_i \boldsymbol{j} \qquad (i = 1, 2, 3) \tag{6}$$

The temperature gradient vector $\boldsymbol{T}'$ is constant over the triangle and expressed by

$$\boldsymbol{T}' = m_2 \boldsymbol{i} + m_3 \boldsymbol{j} \tag{7}$$

If the element has a thickness δ and thermal conductivity k, then using Fourier's law, the heat flow q_i into an element at each boundary element can be evaluated using the dot product of the temperature gradient vector and the edge normal vector:

$$q_i = -k\delta L_i \boldsymbol{T} \cdot \boldsymbol{N}_i(x_{b_i}, y_{b_i}) \qquad (i = 1, 2, 3) \tag{8}$$

Replacing and rearranging the equation,

$$\begin{aligned} q_1 = -k\delta L_1 [&T_{b_1}(c_1 n_{21} + d_1 n_{31}) + T_{b_2}(c_1 n_{22} + d_1 n_{32}) \\ &+ T_{b_3}(c_1 n_{23} + d_1 n_{33})] \end{aligned} \tag{9}$$

Table 3 Material properties used in the model

Material	ρ, kg/m^3	C_p, J/(kg · K)	K, W/(m^2 · K)	Comment
Glass ceramics	2780	810	1.6	Telescope mirror
Be	1850	1820	190	Scan mirror
Invar	8890	512	10.4	Inner baffle, mirror housing
Al	2700	960	165	Spider, flexure
Silicone rubber	850	1331	0.31	Spacer (between mirror and housing)

$$q_2 = -k\delta L_2[T_{b_1}(c_2n_{21} + d_2n_{31}) + T_{b_2}(c_2n_{22} + d_2n_{32}) + T_{b_3}(c_2n_{23} + d_2n_{33})] \tag{10}$$

$$q_3 = -k\delta L_3[T_{b_1}(c_3n_{21} + d_3n_{31}) + T_{b_2}(c_3n_{22} + d_3n_{32}) + T_{b_3}(c_3n_{23} + d_3n_{33})] \tag{11}$$

However, q_i can also be expressed in terms of conductances between the boundary elements, as in Fig. 6:

$$q_1 = g_{1,2}(T_{b_1} - T_{b_2}) + g_{1,3}(T_{b_1} - T_{b_3}) \tag{12}$$

$$q_2 = g_{1,2}(T_{b_2} - T_{b_1}) + g_{2,3}(T_{b_2} - T_{b_3}) \tag{13}$$

$$q_3 = g_{2,3}(T_{b_3} - T_{b_2}) + g_{1,3}(T_{b_3} - T_{b_1}) \tag{14}$$

Equating the preceding two sets of equations yields the expressions for $g_{i,j}$:

$$g_{1,2} = k\delta L_1(c_1n_{22} + d_1n_{23}) \tag{15}$$

$$g_{1,3} = k\delta L_1(c_1n_{23} + d_1n_{33}) \tag{16}$$

$$g_{2,3} = k\delta L_2(c_2n_{23} + d_2n_{33}) \tag{17}$$

This conductance matrix is between the boundary elements only and does not connect them to the center of gravity. It needs to be transformed into a conductance matrix between the element center of gravity and the boundary element, as in Fig. 7. The two conductance matrices are equivalent, but the conductance matrix from the center of gravity has 6 conductances, whereas the matrix between the boundary elements has only 3. It is obvious that the temperature at the center of gravity of the triangle is equal to the average temperature of the midpoints of the sides by assuming the triangle has a linear temperature gradient. It can be deduced that the conductances between the boundary element and the calculation point are equal to each other:

$$G_{1,\mathrm{CG}} = G_{2,\mathrm{CG}} = G_{3,\mathrm{CG}} \tag{18}$$

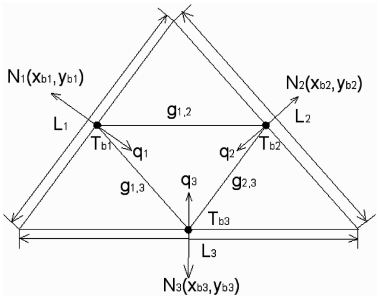

Fig. 6 Conductance matrix between boundary elements for triangular element.

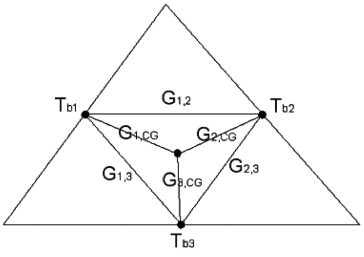

Fig. 7 Conductance matrix between boundary elements and center of gravity for triangular element.

An additional constraint is that the root-mean-square value of the sum of the conductances between the boundary elements is minimized:

$$\frac{\partial(G_{1,2}^2 + G_{1,3}^2 + G_{2,3}^2)}{\partial G_{1,\mathrm{CG}}} = 0 \tag{19}$$

The star-delta transformation is used to provide the other 3 equations:

$$\frac{G_{1,\mathrm{CG}}G_{2,\mathrm{CG}}}{G_{1,\mathrm{CG}} + G_{2,\mathrm{CG}} + G_{3,\mathrm{CG}}} + G_{1,2} = g_{1,2} \tag{20}$$

$$\frac{G_{1,\mathrm{CG}}G_{3,\mathrm{CG}}}{G_{1,\mathrm{CG}} + G_{2,\mathrm{CG}} + G_{3,\mathrm{CG}}} + G_{1,3} = g_{1,3} \tag{21}$$

$$\frac{G_{2,\mathrm{CG}}G_{3,\mathrm{CG}}}{G_{1,\mathrm{CG}} + G_{2,\mathrm{CG}} + G_{3,\mathrm{CG}}} + G_{2,3} = g_{2,3} \tag{22}$$

The conductances between boundary elements and element center of gravity can be achieved through resolving Eqs. (18–22). For tetrahedral elements, the same method mentioned previously can be used to yield sets of equations about the conductances between the boundary elements and the element center of gravity, as in Fig. 8:

$$G_{1,\mathrm{CG}} = G_{2,\mathrm{CG}} = G_{3,\mathrm{CG}} = G_{4,\mathrm{CG}} \tag{23}$$

$$\frac{\partial(G_{1,2}^2 + G_{1,3}^2 + G_{1,4}^2 + G_{2,3}^2 + G_{2,4}^2 + G_{3,4}^2)}{\partial G_{1,\mathrm{CG}}} = 0 \tag{24}$$

$$\frac{G_{i,\mathrm{CG}}G_{j,\mathrm{CG}}}{G_{1,\mathrm{CG}} + G_{2,\mathrm{CG}} + G_{3,\mathrm{CG}} + G_{4,\mathrm{CG}}} + G_{i,j} = g_{i,j} \quad (i, j = 1, 2, 3, 4, i \neq j) \tag{25}$$

The capacitance term is simplified using the assumption of constant density and specific heat c over the control volume region:

$$\frac{dU}{dt} = \rho c V \frac{dT}{dt} \tag{26}$$

The heat balance for control volume i can thus be expressed as

$$Q_i + \sum_{j=1}^{3} G_{j,\mathrm{CG}} \times f(T_i, T_{b_j}) = \rho_i c_i V_i \frac{dT_i}{dt} \tag{27}$$

And the sum of energy flows to the boundary calculation point is zero, which yields a set of algebraic equations for each boundary calculation point. All of these equations mentioned previously can then be solved to determine the temperatures at the control volume calculation points.

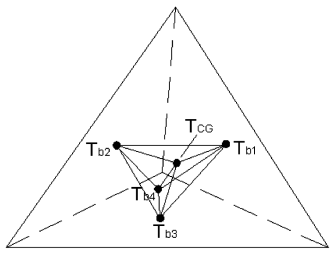

Fig. 8 Conductance matrix between boundary elements and center of gravity for tetrahedral element.

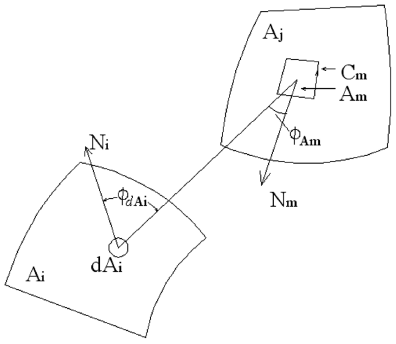

Fig. 9 The two surfaces for the radiation view factor calculation.

IV. Boundary Condition

A. Radiation Heat Transfer Between Surface Elements

Radiation heat transfer can be modeled using Oppenheim's method. With Oppenheim's method, an additional nongeometric boundary element for each radiating element is created, which couples to its parent with a conductance equals to $\sigma A\varepsilon/(1-\varepsilon)$. Then the radiation view factor is used to create couplings between the nongeometric surface elements. It is equal to σAF_{ij}:

$$Q_{ij} = \sigma(T_i^4 - T_j^4) \Big/ \left(\frac{1-\varepsilon_i}{\varepsilon_i A_i} + \frac{1}{A_i F_{ij}} + \frac{1-\varepsilon_j}{\varepsilon_j A_j}\right) \tag{28}$$

where F_{ij} is the radiation view factor from surface i to surface j. Radiation view factors represent that the fraction of the total diffuse radiative energy emitted from a particular surface, which arrives at a second surface, assuming no intermediate reflections, which are functions of the surface geometry only.

$$A_i F_{i,j} = A_j F_{j,i} = \frac{1}{\pi}\int_{A_j}\int_{A_i} \cos\phi_i \cos\phi_j \frac{\mathrm{d}A_i \mathrm{d}A_j}{R^2} \tag{29}$$

There are two methods for computing radiation view factors based on a blockage criterion. When it is established such that there is an unobstructed view for two surfaces, the view factor using the exact contour integral method is computed. This method is very fast and gives accurate results regardless of the surface geometry or size ratio. For surface pairs for which the view is partially obstructed by the other elements, obstruction checks must be performed, and the finite difference method with element subdivision for radiation view factor calculation is used.

Exact contour integral method is simplified in Eq. (29) by Stock's theorem. The radiation view factor from surface $\mathrm{d}A_i$ to surface A_m (surrounded by contour C_m) on A_j, as in Fig. 9:

$$F_{dA_i,A_m} = \frac{1}{\pi}\int_{A_m} \frac{\cos\phi_{dA_1}\cos\phi_{A_m}}{R^2}\mathrm{d}A_m \tag{30}$$

where

$$R^2 = (x_i - x_m)^2 + (y_i - y_m)^2 + (z_i - z_m)^2$$

x_i, y_i, and z_i are coordinates of dA_i; x_m, y_m, and z_m are coordinates of moving point on A_m. Formulation (30) can be expressed as

$$F_{dA_i,A_m} = \int_{A_m} [\cos\alpha_m(x_i - x_m) + \cos\beta_m(y_i - y_m) + \cos\gamma_m(z_i - z_m)] f \mathrm{d}A_m \tag{31}$$

where

$$f = [\cos\alpha_i(x_i - x_m) + \cos\beta_i(y_i - y_m) + \cos\gamma_i(z_i - z_m)]/(\pi L^4)$$

$\cos\alpha_i$, $\cos\beta_i$, and $\cos\gamma_i$ are cosine values of the normal direction of dA_i; $\cos\alpha_m$, $\cos\beta_m$, and $\cos\gamma_m$ are cosine values of the normal direction of the moving point on A_m. Then the formulation (31) can be expressed as

$$\begin{aligned} F_{dA_i,A_m} = {} & \cos\alpha_i \oint_{C_m} \frac{(z_m - z_i)\mathrm{d}y_m + (y_m - y_i)\mathrm{d}z_m}{2\pi R^2} \\ & + \cos\beta_i \oint_{C_m} \frac{(x_m - x_i)\mathrm{d}z_m + (z_m - z_i)\mathrm{d}x_m}{2\pi R^2} \\ & + \cos\gamma_i \oint_{C_m} \frac{(y_m - y_i)\mathrm{d}x_m + (x_m - x_i)\mathrm{d}y_m}{2\pi R^2} \end{aligned} \tag{32}$$

$A_i = \sum \Delta A_i$, $A_j = \sum A_m$, and

$$F_{dA_i,A_j} = \sum_{A_j} F_{dA_i,A_m}$$

Thus, the radiation view factor for the two surfaces can be expressed as

$$F_{A_i,A_j} = \frac{1}{A_i}\sum_{A_i} F_{dA_i,A_j}\Delta A_i \tag{33}$$

The calculation of the radiation view factors for surface pairs for which the view is partially obstructed by other elements involves the following steps. Each surface is subdivided and the accuracy of the calculation is proportional to the granularity of the surface subdivision (the penalty for higher accuracy is increased computation time). For each of the subsurface pairs, an intervening surface is considered to obstruct if it intercepts the line joining the centroids of the two subsurfaces. If obstructing is discovered, the view factor between the two subsurfaces is set to 0. The view factors are calculated between the unobstructed subsurface pairs only:

$$\Delta F_{ij} = \frac{1}{\pi\Delta A_i}\frac{\cos\phi_i\cos\phi_j}{R^2}\Delta A_j A_i \tag{34}$$

Two parallel unit squares separated by a distance of D are used to compare the accuracy of the method adopted in this paper and the Nusselt sphere method with mesh subdivision. As Table 4 shows, the accuracy of the method adopted in this paper is almost independent of the separation of D. The Nusselt sphere method has an error around 11% for the first mesh subdivision and 5% for the second mesh subdivision, when the elements are very close together.

The view factors for all subsurface pairs are summed to obtain the overall view factor and the calculation of the view factors can be very intensive.

B. Heat Flux Calculation

The solar view factors F_s reflect the amount of energy an element receives from the solar source that is modeled as a distant point source for the thermal model:

Table 4 Error (%) vs separation distance D for two parallel unit squares

D	Method A (first mesh subdivision)	Method A (second mesh subdivision)	Method B (first mesh subdivision)	Method B (second mesh subdivision)
0.01	0.001	0.00001	1.7	0.001
0.1	0.0003	0.000002	10.4	4.5
1	0.000005	0.0000006	5.5	1.4
10	0	0	0.09	0.023

[a]Method A is the radiation view factor calculating method adopted in this paper and method B is the Nusselt method.

$$F_s = \frac{A_i' \cos\theta}{A_i} \tag{35}$$

where A_i' is the irradiated area of the element, θ is the angle between the element surface normal and the solar vector, and A_i is the total area of the element.

The unobstructed solar view factors are computed accurately and efficiently using a contour integral algorithm. The solar view factors that are shadowed by intervening elements are handled using element subdivision.

The incident radiation on any element is simply the product of its view factor to the source multiplied by the flux from the source: $Q = F_s \times A_i \times q_s$.

If the incident flux falls on elements that are not perfect absorbers, then some of it will be reflected to other elements in the model. This reflection is modeled using a gray-body view factor approach (Gebhardt's method). Ray-tracing method is used to model the specular reflections.

V. Results and Discussion

The altitude of the orbit is 36,000 km. The velocity of the spacecraft is 0.0044 rad/ min. It takes 24 h (86,400 s) for the spacecraft to travel once around the Earth. There are five typical solar declinations chosen to calculate the temperature of the radiometer. For the solar declination of 0 deg, 4140 s is spent in the Earth shadow region. For the other four solar declinations, all of the time is spent in the sun illumination. Thirty-six evenly distributed calculation positions are added on the orbit. Four calculation positions are added when solving with eclipse. Two are located at the start of the eclipse region and the other two are at its end to capture the rapid heat flux variation that occurs in these regions.

The scan mirror is exposed to the direct view of the sun for approximately 4 h during the local middle night and the deep space during the remaining periods. The collimated solar incident fluxes are the main heat load on the scan mirror. The diffused incident fluxes and the infrared incident fluxes can be omitted in the thermal analysis, as shown in Fig. 10.

A high-emissivity coating is applied on the back of the scan mirror to decrease its average temperature. Figure 11 shows the diurnal temperature variations of the scan mirror. The highest temperature of the scan mirror without coating (mirror back emissivity is 0.7, mirror back absorptivity is 0.7, mirror rib emissivity is 0.7 and mirror rib absorptivity is 0.7) can reach 70°C, and the mirror temperature difference during a single diurnal period can be above 70°C. The highest temperature of the mirror with coating (mirror back emissivity is 0.88, mirror back absorptivity is 0.26, mirror rib emissivity is 0.014, and mirror rib absorptivity is 0.192) can reduce to around 40°C and the mirror temperature difference is nearly 30°C. Figure 12 shows the variational trend of the scan mirror temperature predicted in this paper, which is very close to experimental data in [15]. The scan mirror temperature varies diurnally and it is different for different solar declinations. Figure 13 shows that the peak temperature of the scan mirror occurs when the solar declination is −8.8 deg, which is the same as that mentioned in [16]. Figure 14 shows a comparison of the gradients along the major and the minor axes of the scan mirror. The temperature difference on the major axis is greater than that on the minor axis, because the heat flux variation along the major axes is more obvious.

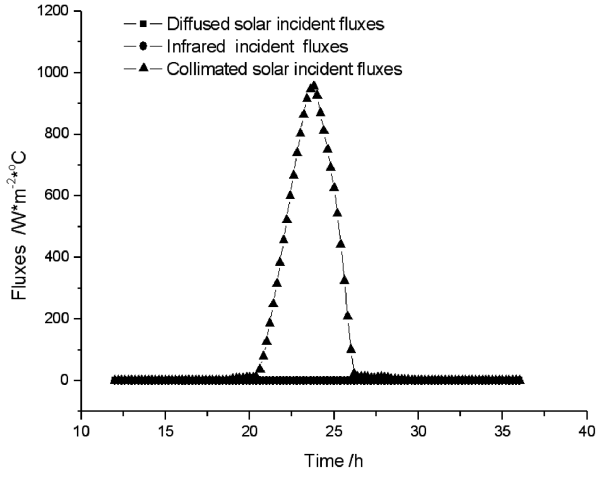

Fig. 10 Heat flux on the scan mirror.

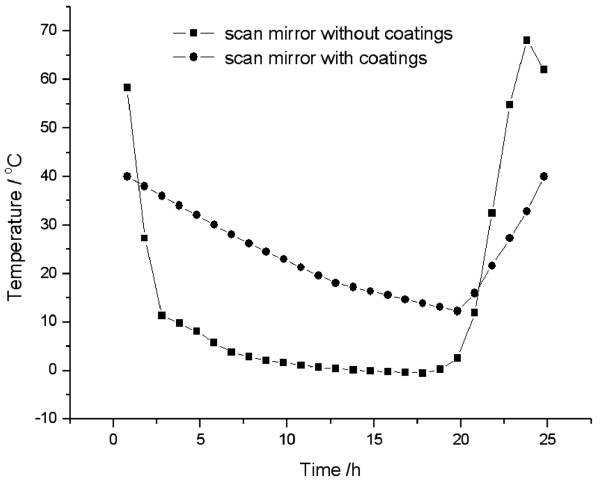

Fig. 11 Temperature variations of the scan mirror in 24 h.

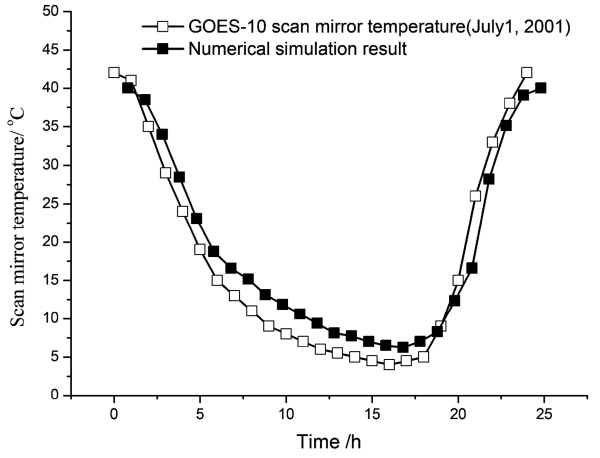

Fig. 12 Comparison between calculating values and experimental values.

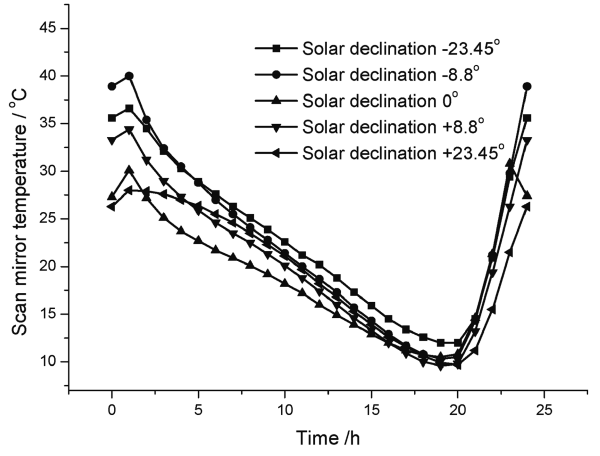

Fig. 13 Temperature variations of the scan mirror for different solar declinations.

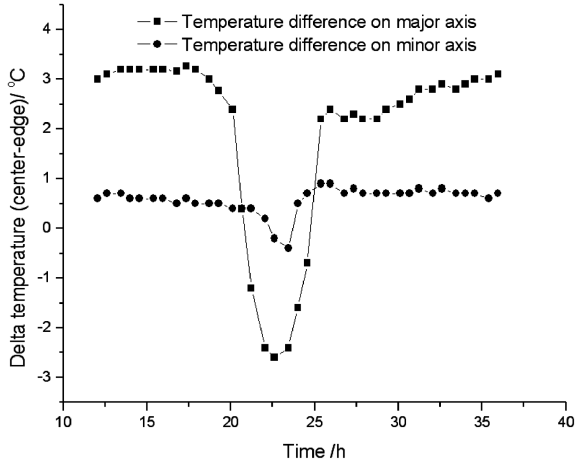

Fig. 14 Temperature differences of the scan mirror in 24 h.

During the period of the local middle night, the impingement of the solar energy is focused, which is reflected by the telescope primary mirror and onto the secondary mirror. The quantity of the flux reaches the highest level when the solar declination is 0 deg; the solar load on the secondary mirror is nearly zero when the solar declination is ± 8.8 and ± 23.45 deg, as shown in Fig. 15. The heat load on the secondary mirror housing and spider is from the fluxes reflected by the scan mirror and the primary mirror. The heat load peak value on the mirror housing and spider reaches the highest level during the period the scan mirror is directly exposed to the direct view of the sun when the solar declination is 0 deg. The total heat load is the highest when the solar declination is 0 deg for the mirror housing. As for the spider, its total heat load reaches the highest when the solar declination is -23.5 deg, as in Figs. 16 and 17, and heat loads on these two components are nearly zero without solar intrusion.

Figures 18–20 present comparisons of the diurnal temperature variations of the secondary mirror assembly. The secondary mirror temperature reaches 77°C during the local middle night, when the solar declination is 0 deg. In [7], the maximum secondary mirror temperature of the GOES-8 is predicted to be as high as 74°C on day 290 in 1994. The mission-allowable secondary mirror temperature is around 52°C. A set of operating constraints should be levied on the radiometer normal operations to limit it from scanning in the

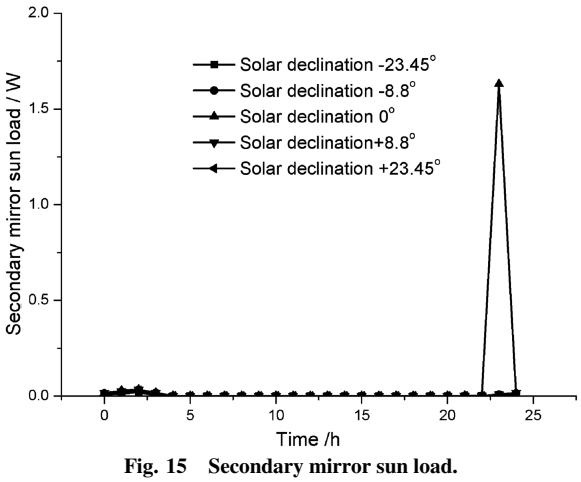

Fig. 15 Secondary mirror sun load.

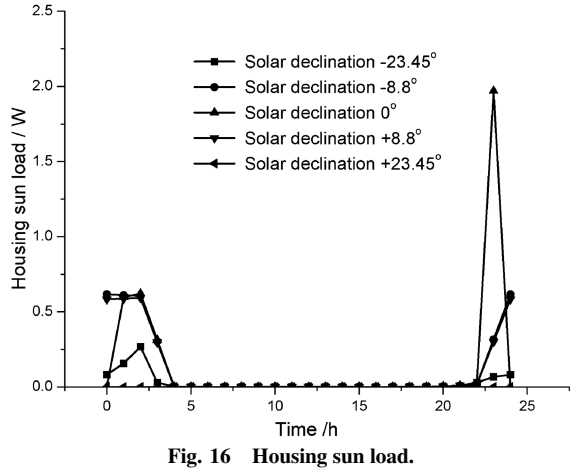

Fig. 16 Housing sun load.

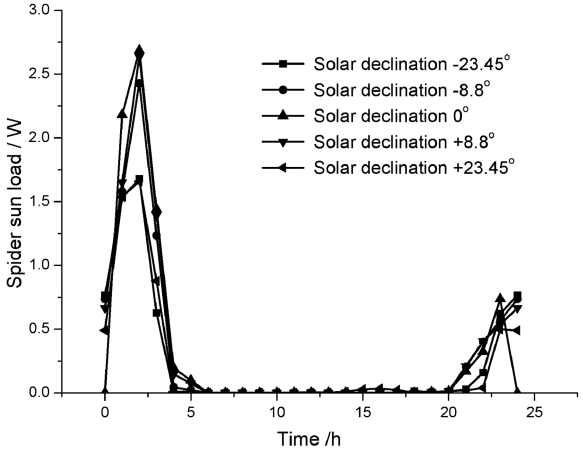

Fig. 17 Spider sun load.

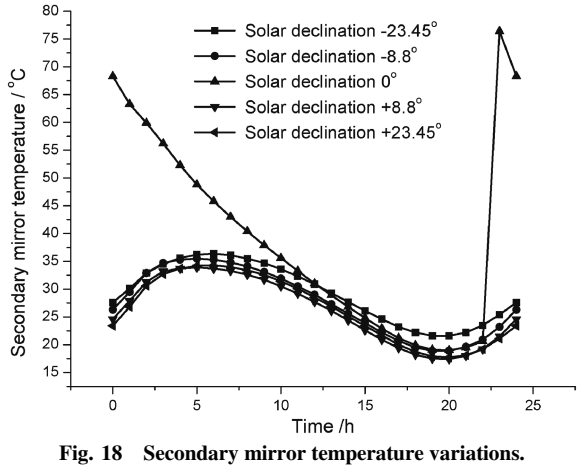

Fig. 18 Secondary mirror temperature variations.

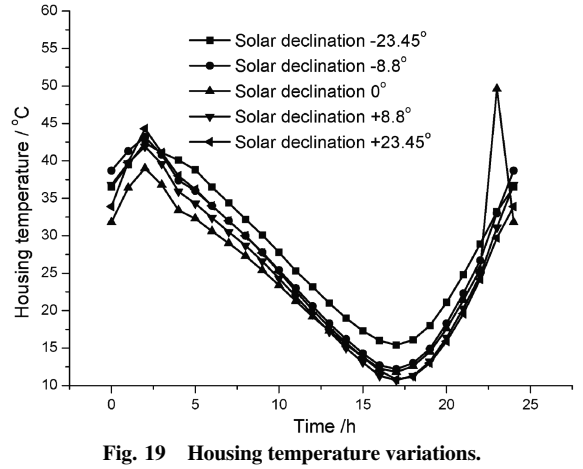

Fig. 19 Housing temperature variations.

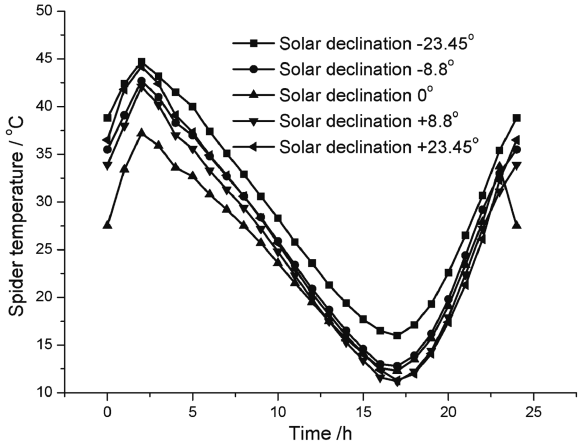

Fig. 20 Spider temperature variations.

vicinity of the sun. The secondary mirror housing and spider temperature reaches the highest when the solar declination is 0 and −23.5 deg, respectively.

VI. Conclusions

A thermal analysis of the radiometer on the FY-4 is performed to determine the health and safety issues with the radiometer operating in the vicinity of the sun. The calculation results show that the scan mirror experiences large temperature excursions during the heating and cooling periods. The control coating applied on the scan mirror back and rib can reduce the temperature variation range effectively, which can reduce the thermal distortion of the scan mirror. The local middle night intrusion increases the temperature of the secondary mirror assembly. All of the preceding results can be used to determine the operational constraints of the FY-4 radiometer instruments.

References

[1] Auternaud, D., and Maute, P., "Earth Observation from Space: from Exploration to Operation," *Alcatel Telecommunications Review*, No. 3, 2003, pp. 285–290.

[2] Hursen, K. A., and Ross, R., "GOES Imager: Overview and Evolutionary Development," *Proceedings of SPIE: The International Society for Optical Engineering*, Vol. 2812, 1996, pp. 160–173. doi:10.1117/12.254064

[3] Murphy-Morris, J. E., and Hinkal, S. W., "GOES Sounder Overview," *Proceedings of SPIE: The International Society for Optical Engineering*, Vol. 2812, 1996, pp. 174–181. doi:10.1117/12.254065

[4] Hinkal, S. W., Jenstrom, D. T., Florez, J., Bremer, J. C., Hersh, M. J., Neuberger, D. E., and Kindsfather, R., "Advanced Geosynchronous Studies Imager: Instrument System Design," *Proceedings of SPIE: The International Society for Optical Engineering*, Vol. 3750, 1999, pp. 2–10. doi:10.1117/12.363510

[5] Neuberger, D. E., Bremer, J. C., and Mehoke, M., "Advanced Geosynchronous Studies Imager Thermal Design," *Proceedings of SPIE: The International Society for Optical Engineering*, Vol. 3750, 1999, pp. 68–78. doi:10.1117/12.363560

[6] Zurmehly, G. E., and Hookman, R. A., "Thermal and Structural Design Constraints for Radiometers Operating in Geostationary Orbits," *Proceedings of SPIE: The International Society for Optical Engineering*, Vol. 1693, 1992, pp. 304–312. doi:10.1117/12.138095

[7] Ghaffarian, B., and Sprunger, K., "Solar Intrusion Thermal Analysis," *Proceedings of SPIE: The International Society for Optical Engineering*, Vol. 2812, 1996, pp. 251–259. doi:10.1117/12.254072

[8] Shen, J. Y., Chen, D. H., and Zhang, Z. M., "Thermal Analysis of an Absolute Radiometer Designed for the Future Satellite Mission of Total Solar Irradiance Measurement," *ASME International Mechanical Engineering Congress and Exposition*, Vol. 364, American Society of Mechanical Engineers, New York, 1999, pp. 189–197.

[9] Mahan, J. R., Kowsary, F., Tira, N., and Gardiner, B. D., "Transient Conduction-Radiation Analysis of an Absolute Active Cavity Radiometer Using Finite Elements," *International Symposium on Thermal Problems in Space-Based Systems*, Vol. 83, American Society of Mechanical Engineers, New York, 1987, pp. 39–47.

[10] Giesen, P., and Folgering, E., "Design Guidelines for Thermal Stability in Opto-Mechanical Instruments," *Proceedings of SPIE: The International Society for Optical Engineering*, Vol. 5176, 2003, pp. 126–134. doi:10.1117/12.510285

[11] Ding, Y., and You, Z., "A Thermo-Optical Analysis Method for a Space Optical Remote Sensor Optostructural System," *Optical Engineering*, Vol. 43, No. 11, 2004, pp. 2730–2735. doi:10.1117/1.1797872

[12] Hookman, R. A., Zurmehly, G. E., and Hodgman. N. S., "Scanning Mirror Design Considerations for a Geostationary Spaceborne Radiometer," *Proceedings of SPIE: The International Society for Optical Engineering*, Vol. 1693, 1992, pp. 318–329. doi:10.1117/12.138097

[13] Zurmehly, G. E., and Hookman, R. A., "Thermal and Structural Analysis of the GOES Scan Mirror's On-Orbit Performance," *Proceedings of SPIE: The International Society for Optical Engineering*, Vol. 1532, 1991, pp. 170–176. doi:10.1117/12.48272

[14] Zhang, J., Zhang, Y., Han, J., He, X., and Yao, W., "Lightweight C/SiC Mirrors for Space Application," *Proceedings of SPIE: The International Society for Optical Engineering*, Vol. 6148, 2006, pp. 61480L1–61480L6.

[15] Wu, X., Weinreb, M., Chang, I. L., Crosby, D., Dean, C., Sun, F., and Han, D., "Calibration of GOES Imager Visible Channels," *2005 IEEE International Geoscience and Remote Sensing Symposium*, Vol. 5, Inst. of Electrical and Electronic Engineers, Piscataway, NJ, 2005, pp. 3432–3435.

[16] Weinswig, S. A., and Hookman, R. A., "Optical Analysis of Thermal-Induced Structural Distortions," *Proceedings of SPIE: The International Society for Optical Engineering*, Vol. 1527, 1991, pp. 118–125. doi:10.1117/12.48643

G. Palmer
Associate Editor